Research Article

Received: 5 May 2023 Revised: 23 June 2023 Accepted article published: 11 July 2023 Published online in Wiley Online Library: 22 July 2023

(wileyonlinelibrary.com) DOI 10.1002/jsfa.12846

Aromatic biomass (torch ginger) leaf-derived three-dimensional honeycomb-like carbon to enhance gravimetric supercapacitor

Erman Taer,[a] Novi Yanti,[a] Elfrida Padang,[a] Apriwandi Apriwandi,[a] Zulkarnain Zulkarnain,[a] Ninis Hadi Haryanti,[b] Mohamad Deraman[c] and Rika Taslim[d*]

Abstract

Background: Porous carbon electrode (PCE) is identified as a highly suitable electrode material for commercial application due to its production process, which is characterized by simplicity, cost-effectiveness and environmental friendliness. PCE was synthesized using torch ginger (*Etlingera elatior* (Jack) R.M. Smith) leaves as the base material. The leaves were treated with different concentrations of $ZnCl_2$, resulting in a supercapacitor cell electrode with unique honeycomb-like three-dimensional (3D) morphological pore structure. This PCE comprises nanofibers from lignin content and volatile compounds from aromatic biomass waste.

Results: From the characterization of physical properties, PCE-0.3 had an impressive amorphous porosity, wettability and 3D honeycomb-like structural morphology with a pore framework consisting of micropores and mesopores. According to the structural advantages of 3D hierarchical pores such as interconnected honeycombs, PCE-0.3 as supercapacitor electrode had a high specific capacitance of up to 285.89 F g^{-1} at 1 A. Furthermore, the supercapacitor exhibited high energy and power density of 21.54 Wh kg^{-1} and 161.13 W kg^{-1}, respectively, with a low internal resistance of 0.059 Ω.

Conclusion: The results indicated that 3D porous carbon materials such as interconnected honeycombs derived from the aromatic biomass of torch ginger leaves have significant potential for the development of sustainable energy storage devices.

Keywords: torch ginger leaves; honeycomb-like 3D; porous carbon; supercapacitor; energy storage

INTRODUCTION

The recent attention paid to the continuous improvement of supercapacitors as electrical energy storage devices, in terms of electrodes and electrolytes, is because of their advanced performance with superior energy and power capacities compared to conventional capacitors and batteries.[1] Some of these innovations include graphene,[2] graphene oxide,[3] activated carbon/porous carbon,[3] carbon aerogel,[4] conductive polymer[5] and metal oxide.[6] Activated carbon materials with unique geometries such as nanofibers,[7] nanotubes,[8] nanoballs,[9] nanosheets[10] and nano-3D[11] have become of interest due to their thermal stability and electrochemical conductivity.[12,13] Three-dimensional (3D) activated carbon materials with connected hierarchical pores have shown great potential because of their superior microstructure with adjustable porosity and excellent electrochemical performance.[12,14] The production of activated carbon with a 3D pore structure has been carried out through simple, uncomplicated and time-consuming approaches, including carbonization, chemical activation and physical activation.[15]

Previous studies have demonstrated that 3D hierarchically interconnected porous activated carbon rich in micropores can be produced from biomass waste materials using simple methods, leading to improved electrochemical performance.[16,17] The selection of biomass as the base material for supercapacitor electrodes is driven by global concerns about creating sustainable technologies.[18] This is due to its abundant presence, natural microporous structure and environmental friendliness as an electrical energy storage device.[19] Aromatic biomass with a distinctive odor, resulting from its lignin content and volatile compounds, composed of abundant aromatic structures has become the focus of attention in this field.[20] For example, Cao *et al*.[21] used a popular

* *Correspondence to: Rika Taslim, Department of Industrial Engineering, State Islamic University of Sultan Syarif Kasim Riau, 28293 Simpang Baru, Riau, Indonesia, E-mail: rikataslim@gmail.com*

a *Department of Physics, University of Riau, Pekanbaru, Indonesia*

b *Department of Physics, University of Lambung Mangkurat, Banjarmasin, Indonesia*

c *School of Applied Physics, Faculty of Science and Technology, Universiti Kebangsaan Malaysia, Bangi, Malaysia*

d *Department of Industrial Engineering, State Islamic University of Sultan Syarif Kasim Riau, Pekanbaru, Indonesia*

sawdust waste with abundant aromatic structures to produce a 3D carbon skeleton with improved porosity and specific capacitance. Taer *et al.*[22] also considered using citronella leaves as an aromatic biomass-based carbon precursor to produce a 3D interconnected porous carbon with high electrochemical performance through a one-step integrated pyrolysis process (physical carbonization–activation) with $ZnCl_2$ impregnation.

The study reported here focused on using aromatic biomass waste, obtained from agricultural residues rich in lignin, cellulose, hemicellulose and volatile elements, as the base material for producing porous carbon for supercapacitor electrodes. Torch ginger leaves were selected as an example of potential agricultural waste for this purpose. In a previous report, torch ginger plant parts, namely flowers, rhizomes, leaves, bark, stems and roots, were optimized as natural antioxidants and antibacterial agents.[23–26] However, the use of torch ginger leaf wastes as a material for making porous carbon, especially for electrodes in supercapacitor cell components, is still in its early stages.[27,28] Torch leaves have a characteristic dark-green color and are 80 cm × 18 cm. They are a good source of carbon-producing nanocellulose[29] and the conversion into 3D porous activated carbon is simple and uncomplicated. The process involves continuous carbonization and physical activation to produce activated carbon with a honeycomb-like hierarchical pore structure rich in interconnected micropores.

The activated carbon was produced from aromatic biomass waste from renewable torch ginger leaves, using a simple and harmless one-stage integrated pyrolysis process (carbonization–physical activation). The 3D porous honeycomb structure was obtained based on different activator concentrations. Chemical activation was done using $ZnCl_2$ with low concentrations (0.1, 0.3, 0.5 and 0.7 mol L^{-1}) mixed with torch ginger leaf carbon through a chemical activation process, which contributed to controlling the formation of pore structures. In this process, no complicated and very tedious template methods were required to produce interconnected pore microstructures. The increase in specific capacitance and energy and power densities of the obtained porous carbon electrode (PCE) was also supported by the attractive features of the hierarchical pore system. This included good amorphous properties, high wettability and provision of active sites between the electrode and suitable electrolyte during the electrochemical process. The selection of the precursor of the aromatic biomass of torch ginger leaves as a material for making carbon electrodes was a very suitable and promising strategy for sustainable, renewable, environmentally friendly and cost-effective energy storage devices.

MATERIALS AND METHODS

Basic materials

An amount of 5 kg of torch ginger harvest waste in the form of old leaves was collected from community plantations in Pekanbaru, Riau. The green-brown leaves with a distinctive aroma were cut to <5 cm to make processing easier. Subsequently, the samples were dried in the sun and an oven for 5 days to dehydrate them.

Additional materials

The torch ginger leaf waste was treated to create a porous carbon base material for supercapacitor electrodes using $ZnCl_2$ impregnation at different concentrations of 0.1, 0.3, 0.5 and 0.7 mol L^{-1}M as an activating agent. A total of 1 mol L^{-1} H_2SO_4 was used as a source of electrically charged ions to fill the carbon pores. The acidity level of the samples was measured using pH indicator strips. These three materials were purchased from Merck KgaA, Germany. Chemical activation and sample neutralization were carried out by adding distilled water as an activator solvent and sample purification.

Electrode manufacturing

The dried torch ginger leaves were pre-carbonized by heating at a temperature of 250 °C for 2.5 h to brittleness and producing charcoal. Subsequently, the carbon was ground to a particle size of <60 μm using mortar and ball milling. The samples were chemically activated with $ZnCl_2$ at concentrations of 0.1, 0.3, 0.5 and 0.7 mol L^{-1} using a Thermo Scientific hot plate stirrer at 80 °C and 300 rpm rotation. This process was begun by dissolving the $ZnCl_2$ activator with distilled water for 1 h, followed by mixing 30 g of carbon and stirring for 2 h. The carbon of activated torch ginger leaves was heated in an oven for 2 days to rehydrate the remaining water content during chemical activation. The samples were printed into coins with a solid texture and not brittle using a hydraulic press at a pressure of eight tons with a holding time of 2 min. A unique honeycomb-like 3D hierarchical pore structure rich in interconnected micropores was generated through one-stage integrated pyrolysis, namely carbonization and physical activation using a Payuntech furnace. Carbonization was carried out from room temperature to 600 °C under the influence of nitrogen gas to vaporize elements other than carbon in the sample. This was followed by physical activation up to a temperature of 850 °C under the influence of carbon dioxide gas to open the pore structure of the carbon. Finally, each sample was neutralized (pH = 7) using distilled water with a scale-washing technique to characterize its physical and chemical properties. Figure 1 shows a schematic of the preparation of supercapacitor PCEs based on torch ginger leaf aromatic biomass with high potential for further development.

Physical characterization

The basic physical properties of PCEs based on torch ginger leaves were determined through the amount of density reduction before and after N_2/CO_2 pyrolysis. This was based on the calculation of the mass, diameter and thickness of PCE coins by measuring carbon coins using digital scales and a caliper. The functional groups and wettability level of activated carbon was investigated with Fourier transform infrared (FTIR) characterization using a Shimadzu Prestige 21 Nicolet Avatar 360 IR with an infrared light source. Subsequently, the degree of crystallinity of carbon samples was determined through X-ray diffraction (XRD) characterization using a Merck Panalitical Philip X-Pert PRO PW 3060/10 with a Cu-Kα radiation source. This was followed by the determination of the morphological appearance of carbon coins through scanning electron microscopy using a Zeiss EVO 10 vacuum at room temperature (24 °C) with secondary electron reflection. The specific surface area and pore size distribution of activated carbon coins were also calculated using the Brunauer–Emmett–Teller (BET) and Barret–Joyner–Halanda (BJH) methods with a Quantachrome Touchwin V1.22 instrument at 300 °C with a flow of 10 °C min^{-1} for 60 min under the influence of absorbed nitrogen gas.

Electrochemical characterization

The electrochemical properties of PCEs based on torch ginger leaves were determined using cyclic voltammetry (CV) and galvanostatic charge–discharge (GCD) methods. This was carried out to evaluate the performance and electric charge storage capacity of

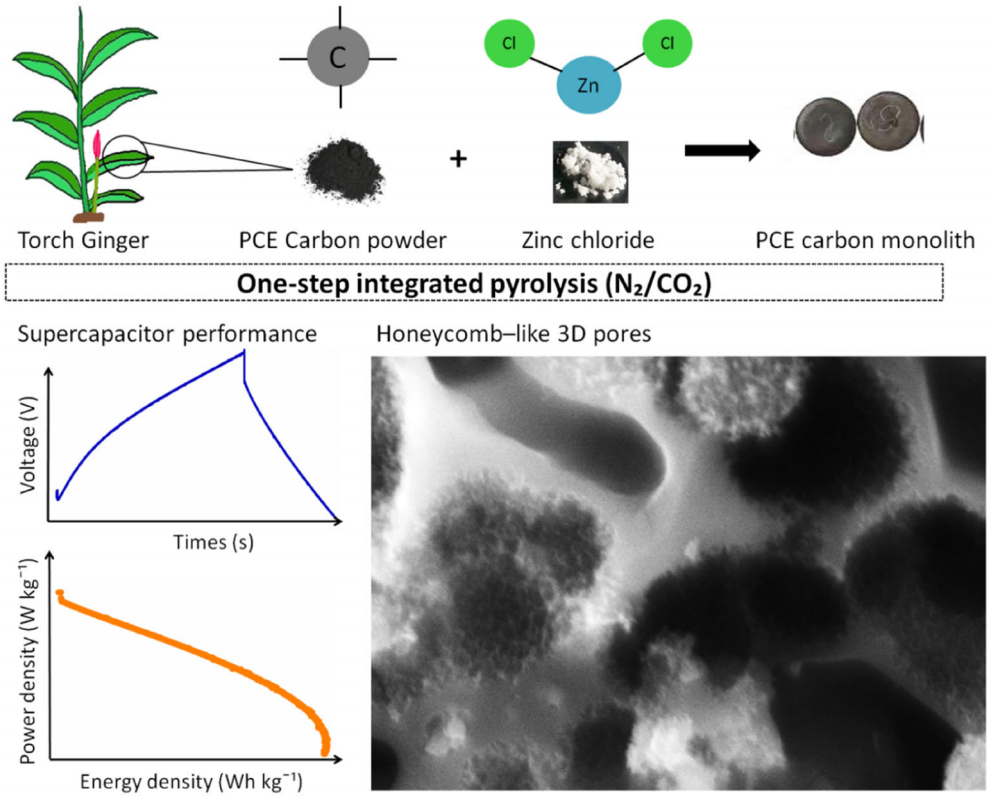

Figure 1. Schematic of PCE preparation with 3D pore structure that supports supercapacitor performance.

the porous carbon. The CV characterization was performed with the physics tool CV UR Rad-Er 5841 Software Cyclic Voltammetry CV V6 calibrated with VersaStat II (Princeton Applied Research) with an error of ±6.0% and GCD using CD UR Rad-ER 2018. This characterization used two electrodes under the influence of aqueous electrolyte. This included 1 mol L^{-1} H_2SO_4 which was separated from the duck eggshell membrane with high resistivity and conductivity. The test was carried out at a potential window of 0–1 V and a low scan rate of 1 mV s^{-1}.

RESULTS AND DISCUSSION

Material properties analysis

One-step integrated pyrolysis of N_2/CO_2 up to a high temperature of 800 °C, through the impregnation of low $ZnCl_2$ concentrations of 0.1, 0.3, 0.5 and 0.7 mol L^{-1} was the first determinant of carbon purity and the formation of pore structures. This was based on density shrinkage, leading to an increase in the porosity of PCE monolithic carbon. The decrease in density after the pyrolysis process was indicated by the evaporation of impurities other than carbon, as confirmed by a reduction in the mass, diameter and thickness of the monolith PCE coins. Based on the decrease in the density of PCE coins as illustrated in Fig. 2, a significant difference was identified in each sample, namely PCE-0.1, PCE-0.3, PCE-0.5 and PCE-0.7. Before pyrolysis, the density values for all samples were almost the same (0.91, 0.99, 0.99 and 0.97 g cm^{-3}) with an average error of 0.036. Meanwhile, the pyrolysis of N_2/CO_2 led to a varying decrease in density of 0.77, 0.61, 0.72 and 0.68 g cm^{-3} with an average error of 0.048. The addition of $ZnCl_2$ from 0.1 to 0.3 mol L^{-1} to the PCE sample increased the density by 39%. This was due to the chemical reaction between $ZnCl_2$

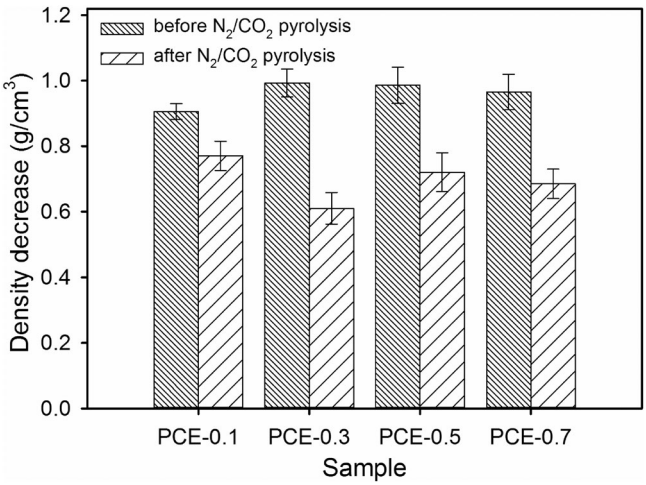

Figure 2. Porosity of PCE monolith coin based on density shrinkage.

and carbon which contributed to the formation of pores during pyrolysis.[30] $ZnCl_2$ reacted with water molecules in the carbon sample to form $ZnCl_2{\cdot}nH_2O$ and the water evaporated during the pyrolysis process as the temperature increased. The formed oxychloride compound reacted with elemental oxygen in the sample to form ZnOCl·*n*Cl, where the elemental chlorine will evaporate during physical activation at high temperatures.[31] The ZnOCl compound decomposed again into ZnO·*n*Cl and the elemental chlorine also evaporated, indicating a reduction in density, thereby increasing the porosity of the sample.[32] This ZnO compound facilitated the formation of pores in carbon materials by

impregnation of $ZnCl_2$.[33] Subsequently, CO_2 by-products evaporated when high-temperature pyrolysis produced space (pores/cavities) and a large specific surface area.[34,35] This was in line with the improved performance of the PCE-0.3 electrode in storing charged ions and the high specific capacitance.[36] The addition of $ZnCl_2$ activator concentration from optimum conditions up to 0.7 mol L^{-1} in PCE samples was also discovered to reduce density loss. This was due to the decomposition of carbon through a direct reaction between the activating agent and excess carbon during pyrolysis, as shown by a decrease in density loss from 39% to 27%. Similarly, related investigations on the decrease in density were also carried out using different biomass such as banana stem waste,[37] solanum torvum fruit[38] and yellow mangosteen fruit.[39]

The functional groups and wettability of activated carbon in torch ginger leaves were analyzed using FTIR spectroscopy through absorption peaks at wavenumbers 450–4450 cm^{-1} as shown in Fig. 3. The peaks of PCE samples experienced a slight shift due to the availability of chemical bonds between functional groups. The results were not the same for each variation of $ZnCl_2$ impregnation concentrations of 0.1, 0.3, 0.5 and 0.7 mol L^{-1}. This aligned with previous reports from different biomass base materials such as date palm tree[40] and annatto peels.[41] All samples showed the presence of wide strain between wavenumbers 3565–3903 cm^{-1} indicated by the primary amine (N—H) and hydroxyl (O—H) functional groups. Based on Fig. 3, it was discovered that low concentrations of $ZnCl_2$ activator can provide optimum hydroxyl groups for PCE samples, while further addition of 0.7 mol L^{-1} will cause a significant reduction. The high concentration of $ZnCl_2$ led to excessive evaporation, which impaired the purity of the carbon, as indicated by the analysis of density reduction. A high content of hydroxyl bonds in activated carbon can cause redox reactions, indicating pseudo-capacitive properties during electrochemical processes. This was because the hydroxyl group was a contribution from the structure of cellulose and hemicellulose, the main constituent of biomass. The primary amine functional group can produce the wettability properties of the PCE electrode and also contribute to increasing ion diffusion at the electrode interface. Furthermore, at wavenumbers 2177–2360 cm^{-1}, there was a strain in all samples as indicated by the strain of the C≡C functional group which showed high carbon purity. At 1450–1600 cm^{-1}, there were strain peaks for all sample variations, attributed to volatile aromatic compounds in the natural content of torch ginger leaves. Phenols and alcohols were also evident from stretching of the C—O functional group at wavenumbers 1152–1287 cm^{-1}.[42] Moreover, the remaining oxygen in the sample can act as a self-doping heteroatom to improve the electrochemical performance of the electrode.

The degree of crystallinity of the PCE samples was analyzed using the XRD method at a scattering angle of 2θ of 10–60°. The characterization results were processed using Microcoral Origin software to obtain lattice parameter values and diffraction patterns. The XRD results for the PCE samples showed two broad peaks and several sharp peaks, as presented in Fig. 4. The broad peaks at diffraction angles of 22–25° and 42–45° in the *hkl* planes (002) and (100) confirmed the presence of a turbostratic structure in form of carbon, which was disturbed due to the formation of pore structures and produced good amorphous properties.[43] Reflection (002) confirmed the availability of weak carbon structures, while 100 indicated the hexagonal structure of the PCE sample. The diffraction pattern of PCE had almost the same appearance as that of previous investigations using different biomass such as wheat husk[44] and camellia pollen.[45] Furthermore, there are several sharp peaks in Fig. 4, indicating the presence of crystalline non-carbon elements as impurities in the sample. Non-carbon elements such as oxygen and nitrogen detected during FTIR testing included natural compounds that make up torch ginger leaves. This was confirmed by JCPDS card no. 82-1690, which showed the presence of calcium atoms in the bonds of the $CaCO_3$ compound in the form of sharp peaks at diffraction angles of 37° and 39°. For further information, JCPDS card no. 89-1668 indicated the presence of silica and oxygen atoms in the form of SiO_2 compounds at angles of 27° and 29°. Meanwhile, the crystal elements in PCE samples were only available in small quantities. This indicated that PCE samples have good availability of amorphous structures for electrodes in supercapacitors.

Table 1 presents the shift in the diffraction angle for each PCE sample based on variations in $ZnCl_2$ activator concentration due to the rearrangement of the porous carbon atom structure back to its initial state during the pyrolysis process. The addition of $ZnCl_2$ at concentrations from 0.1 to 0.3 mol L^{-1} widened the diffraction peaks of 002 and 100, and also increased the amorphous porosity. This was due to the hierarchical formation of

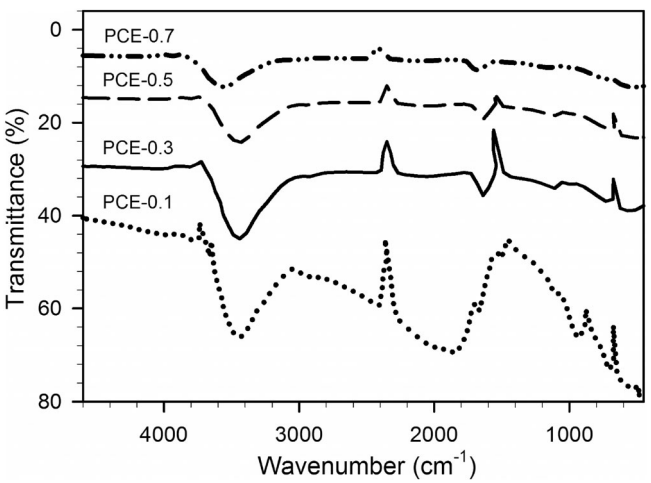

Figure 3. FTIR spectra for all concentration variations of PCE samples.

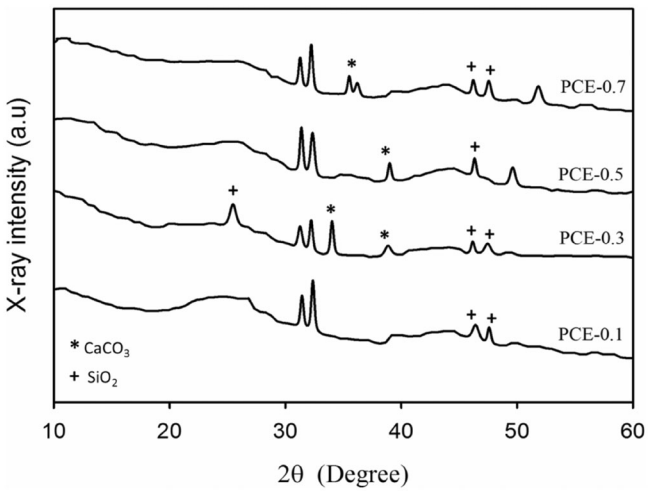

Figure 4. XRD curves of all variations of PCE samples.

micro-, meso- and macropore structures on the surface of the PCE-0.3 coin. Moreover, d_{002} for the PCE sample was greater than the value of $d_{graphite}$ = 3.33 Å,[46] indicating the good properties of amorphous carbon possessed by PCE samples. The d_{100} also confirmed the value that described the carbon characteristic for biomass material.[47] The microcrystalline layer height (L_c) in the PCE samples showed different values for each variation, indicating the more possible microcrystalline layers available in PCE coins. It was also discovered that thinner layers can increase the surface pores in each microcrystalline layer. Furthermore, a small L_c will produce activated carbon with a higher surface area.[48] Optimizing the porosity of the electrode surface also increased the performance of the supercapacitor through electrically charged ion storage spaces/pores, causing an increase in the amount of ionic charge stored in the electrodes.[49] The addition of the $ZnCl_2$ activator to the PCE-0.3 electrode at 0.5 and 0.7 mol L^{-1} can narrow the diffraction angle, which was around 25–44°. This also caused an increase in the value of L_c, indicating that the surface area of PCE-0.3 was larger than that of PCE-0.5 and PCE-0.7.

The morphological structure of the PCE samples was clarified at optimum conditions (PCE-0.3) produced by one-step integrated pyrolysis (N_2/CO_2) using scanning electron microscopy to further highlight the structural advantages of the electrodes. These results revealed an outstanding morphology such as 3D hierarchical fibers and pores, as shown in Fig. 5. Torch ginger leaves with a high natural content of cellulose and lignocellulose produced a very clear fiber morphological structure. Meanwhile, the volatile

Table 1. XRD parameters of all variations of PCE samples

Sample	$2\theta_{002}$ (°)	$2\theta_{100}$ (°)	d_{002} (Å)	d_{100} (Å)	L_c (Å)	L_a (Å)
PCE-0.1	25.122	44.469	3.542	2.036	15.878	32.147
PCE-0.3	24.418	44.616	3.642	2.029	9.235	20.383
PCE-0.5	25.740	44.758	3.458	2.023	12.965	40.774
PCE-0.7	25.182	44.213	3.533	2.047	13.669	34.306

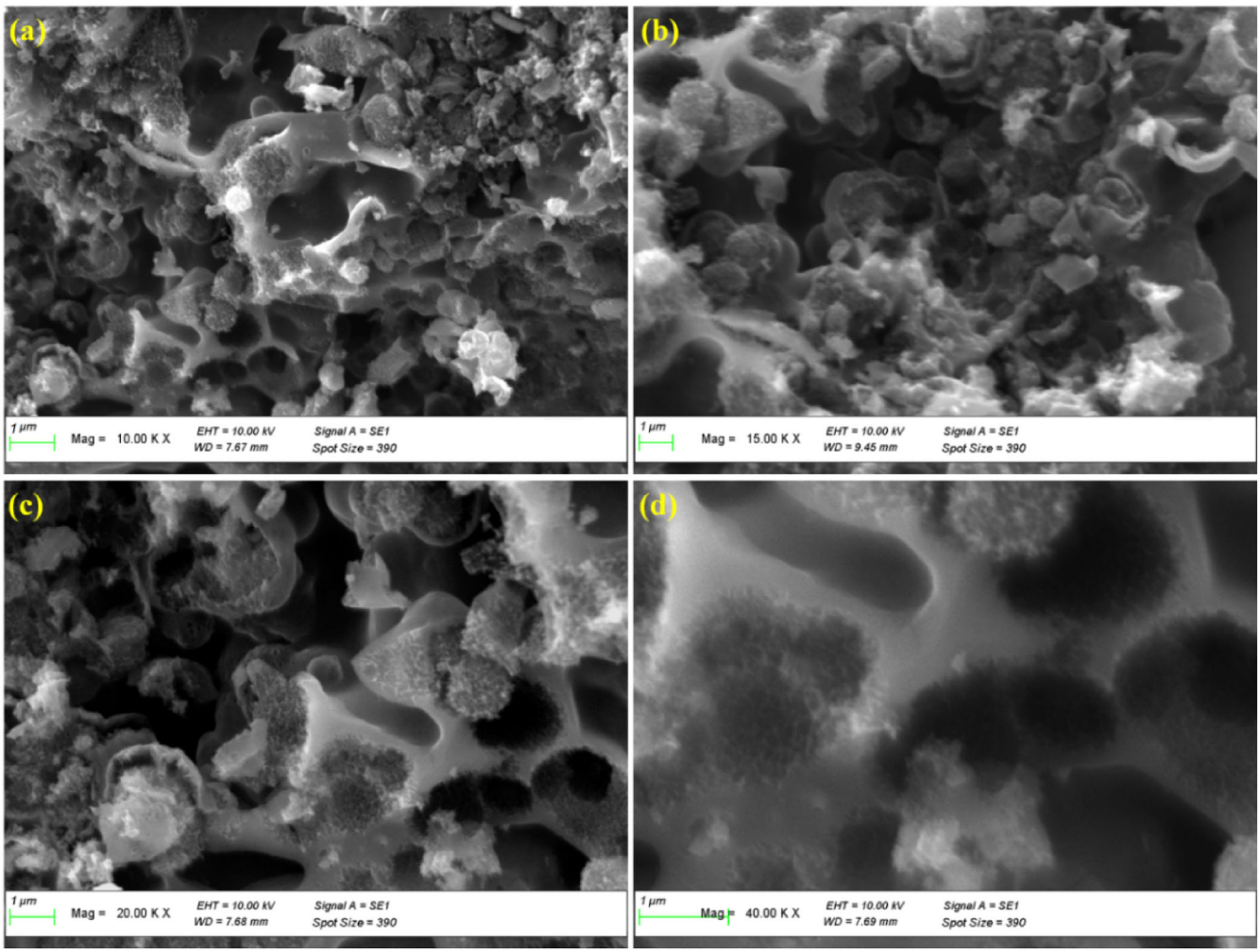

Figure 5. Optimization of the honeycomb-like 3D hierarchical pore morphology structure of PCE-0.3.

compounds giving the distinctive aroma of the leaves can also produce a different morphological appearance.[50,51] At temperatures below 300 °C, it was discovered that volatile compounds created an optimum orderly hierarchical pore structure.[52]

The PCE-0.3 sample which was effected by the $ZnCl_2$ activator at a low concentration of 0.3 mol L^{-1} exhibited unique honeycomb-like 3D hierarchical pores with pore walls composed of very fine nanofiber bundles. The uniqueness of the 3D pore structure in PCE-0.3 greatly impacted the process of electrolyte ion diffusion and electron transfer when applied to supercapacitors.[53] The unique morphology of PCE-0.3 can be fully identified using a high resolution of 10 000×, 150 000×, 20 000× and 40 000×. This was carried out to observe the pore structure on a rougher surface with clearer mesopores, which was important for the high performance of the supercapacitor. In Fig. 5(a)–(d), focus on hierarchical pore structures such as honeycomb is confirmed to have a pore framework thickness ranging from 25 to 48 nm (mesopores) which is composed of very fine fiber walls of less than 2 nm (micropores). Subsequently, no pore collapse was found in the 3D pore structure such as the PCE-0.3 honeycomb sample, indicating an excellent carbon structure with high-purity carbon.[54] The superior conducting path of PCE-0.3 was confirmed through the appearance of a continuous pore structure free of junctions which was also advantageous for the occurrence of ion transport. This was achieved through the use of 0.3 mol L^{-1} $ZnCl_2$ which was most suitable for torch ginger leaf waste-based carbon to increase the specific surface area with a greater number of pores during the one-stage integrated pyrolysis process (N_2/CO_2).[55] It was discovered that a high specific surface area, rich pore count[56] and interconnected pore structure can enhance sufficient active sites in ion adsorption and electron transport. This can cause an increase in the specific capacitance value of the PCE-0.3 electrode.

The absorption ability of PCE samples was analyzed using N_2 absorption–desorption at 77 K through the specific surface area, total volume and pore size distribution. Based on the shapes of the curves in Fig. 6, the PCE obtained through the one-step integrated pyrolysis of N_2/CO_2 up to a high temperature of 800 °C showed a mixed isotherm type of curve between types I and IV, according to IUPAC classification. At a low relative pressure (P/P_0) below 0.3, the amount of adsorbed N_2 increased significantly in all variations of PCE samples. This condition explained the dominant filling of micropores on the surface of the samples.[57] The PCE produced based on the different concentrations of the $ZnCl_2$ activator of 0.1, 0.3, 0.5 and 0.7 mol L^{-1} showed optimum conditions for PCE-0.3. At low concentrations, i.e. PCE-0.1, the worst uptake of N_2 with a much different appearance of the absorption–desorption curve was obtained. Furthermore, the pore volume of PCE-0.1 was very small with very few micropores and mesopores. The addition of the $ZnCl_2$ activator at optimum concentration, confirmed through the PCE-0.3 sample, produced an isothermal curve with a closed hysteresis loop and a surface area of 519.02 m^2 g^{-1} with a high pore volume. PCE-0.3 had a maximum combined micro- and mesoporous pore structure that enhanced the compatible active sites between electrode and electrolyte. Moreover, in detail, the isotherm curves for PCE-0.3, PCE-0.7 and PCE-0.9 samples showed a distortion hysteresis curve (not closed). This is due to the presence of ink-bottle-shaped and numerous narrow-neck pores. Furthermore,

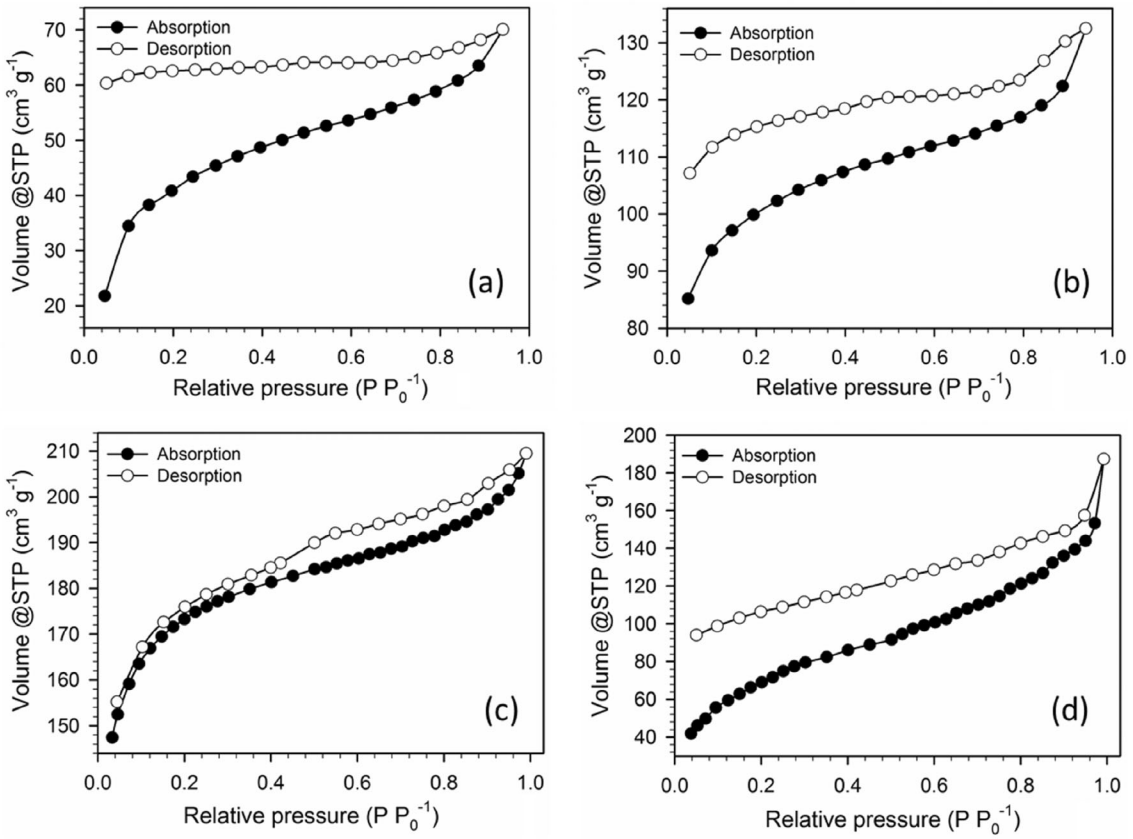

Figure 6. Isothermal curves of PCE samples based on adsorbed N_2 gas.

this is because the more intense chemical reactions of $ZnCl_2$ with biochar allow the widening of the micropore structure to initiate the formation of mesopores. Their disrupted pore dilation structure produces a labile pore shape resembling a bottle-top surface with a thin pore neck. The unique shape of the narrow pore neck with the wide inner surface resists the escape of N_2 gas resulting in the characteristic open-loop hysteresis. The open-loop hysteresis indicated the highest pore widening structure. This large pore structure contributes significantly to favorable electrolyte insertion and rapid ion diffusion in symmetric supercapacitors.

Figure 7 shows the pore distribution of each activated PCE. It was discovered that PCE-0.3 contained a wide range of mesopores (>2 nm) and a hierarchical fiber-combined 3D pore structure rich in interconnected micropores, making it more conducive to the storage of electrically charged ions. N_2 gas absorption parameters such as surface area, pore volume and pore size are presented in Table 2. The relatively low specific surface area value of PCE samples compared to those of the literature can be explained by the very low concentration of $ZnCl_2$ activator (0.1, 0.3, 0.5 and 0.7 mol L^{-1}), which influenced the combination of size and surface pore distribution. Previous reports have shown that optimal micropore–mesopore availability can help facilitate charge transfer during the working process of a supercapacitor.[58]

The capacity and performance of supercapacitors as energy storage devices were determined using CV characterization through a review of specific capacitance, energy density and power density. The measurement was conducted using a symmetric two-electrode carbon system based on torch ginger leaves in a strong acid aqueous electrolyte (1 mol L^{-1} H_2SO_4). Generally, supercapacitors store energy in the form of charged ions from

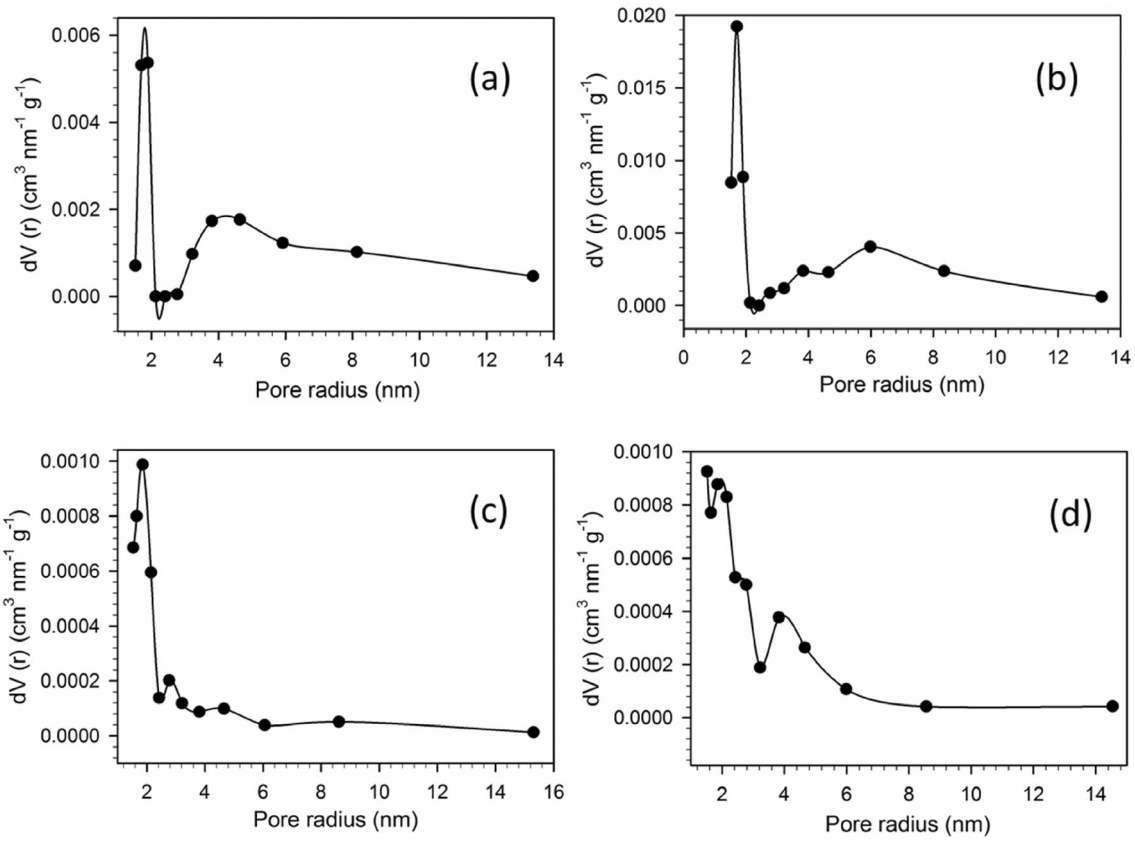

Figure 7. Pore distribution of PCE samples.

Table 2. Parameters of specific surface area of PCE-0.3 sample and comparison with other samples

Source	S_{BET} (m^2 g^{-1})	S_{micro} (m^2 g^{-1})	S_{meso} (m^2 g^{-1})	V_{TOT} (cm^3 g^{-1})	V_{micro} (cm^3 g^{-1})	V_{meso} (cm^3 g^{-1})	D_{ave} (nm)	Ref.
Lacquer wood	1609.09	463.59	1145.5	1.467	0.035	1.432	—	59
Chingma abutilon seed	580.34	316.47	263.87	0.440	0.347	0.093	4.38	60
Cork	710.5	549.7	160.8	0.369	0.236	0.133	2.08	61
Composite of palm	673	375	298	0.19	0.09	0.10	2.04	62
Trichoderma	3977.3	—	—	2.215	1.062	1.153	2.214	63
Native European deciduous trees	616	—	—	0.564	0.274		4.6	64
PCE-0.3	519.02	427.710	91.311	0.324	0.225	0.099	2.500	This study

decomposed electrolytes that move to fill the electrode pores. The energy storage process occurs because of the applied potential difference for a high current to appear when the ions move to fill the electrode pores. This assay was carried out at a fixed scan rate of 1 mV s^{-1} to increase the voltage from 0 to 1 V. Figure 8 displays the CV curves for all the various PCE samples. It was discovered that the imperfect rectangular shape of the curve originated from the combined effect of the electrostatic charge storage mechanism and the surface redox reaction of self-doping heteroatoms.[65,66] The appearance of this curve was an ideal form of electric double-layer supercapacitor (EDLC) for biomass-based electrodes. Characterization was carried out using the CV UR Rad-ER 6841 Physics tool with VersaStat II (Princeton Applied Research) calibration with an error of ±6%. The energy storage process occurred when a voltage of 0–1 V was applied to the electrode, causing ions to fill the pores of the electrode. Meanwhile, discharge occurred when the electrode voltage was biased backward to force the ions out of the carbon pores until the voltage returned to its initial value. A $ZnCl_2$ activator concentration of 0.1 mol L^{-1} can produce a specific capacitance value of 76.43 F g^{-1}. The addition of the activator at 0.3 mol L^{-1} can present a slight bump in the potential area of 0.4–0.8 V. This confirmed the presence of pseudocapacitance which contributed directly to increasing the specific capacitance value significantly almost threefold to 217.42 F g^{-1}. This pseudocapacitance property, ascribed to the presence of the functional groups of O and N, leads to an apparent capacitance,[67] as confirmed through FTIR analysis, that increased the wettability of the carbon material. This maximum result was also supported by the excellent porosity and amorphous properties of the PCE-0.3 sample. The addition of activator concentration up to 0.7 mol L^{-1} reduced the capacitance of activated carbon to 124.55 F g^{-1}. This was because the addition of further concentrations reduced the physical properties of the electrode, such as carbon content and surface area. This indicated that the PCE-0.3 sample had the optimum specific capacitance value for the torch ginger leaves with an activator concentration of 0.3 mol L^{-1} $ZnCl_2$.

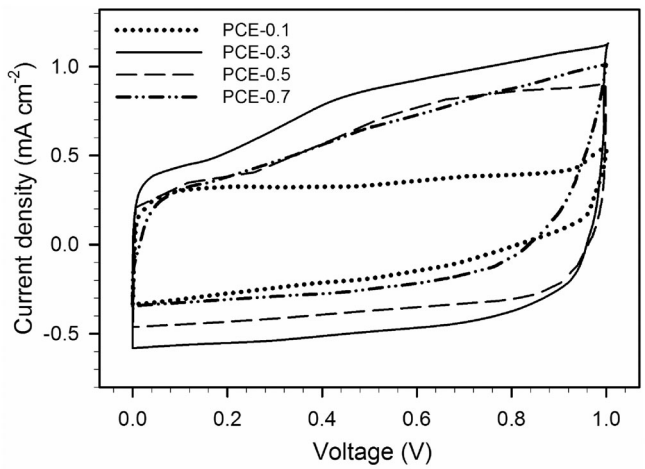

Figure 8. Distorted rectangular CV curves of PCE samples.

Further analysis of the optimization of PCE electrochemical capabilities was carried out using the CV method, at different scan rates of 1, 2 and 5 mV s^{-1}. It was discovered that the CV curve still maintained a rectangular shape. As the scan rate increases to 5 mV s^{-1}, the CV curve displayed a reduced (distorted) rectangular shape. This indicated insufficient response for electrolyte ions to maximally diffuse into the electrode pores at high scan rate,[68] which affected the specific capacitance as presented in Fig. 9(a). Therefore, at a scan rate of 5 mV s^{-1}, the bulge of the pseudocapacitance from the faradaic redox reaction began to weaken and cannot be observed clearly in the electrode material.[69] The reduction in specific capacitance values as the scan rate increased is also presented in Fig. 9(b). This was indicated by charged ions originating from the decomposed electrolyte, namely positive ions (H^+) and negative ions (SO_4^{-2}) that entered with difficulty the electrode pores.[70] According to Brunce Dunn, scan rate and current density response read at a certain voltage had a quantitative relationship that affected the specific capacitance.[71]

The performance of PCE-0.1, PCE-0.3, PCE-0.5 and PCE-0.7 electrodes was evaluated using the GCD method on a symmetric supercapacitor assembled in a two-electrode system at a low current of 1 A. The electrodes were placed in an acidic environment of 1 mol L^{-1} H_2SO_4, an aqueous electrolyte. The GCD curves of the PCE with all $ZnCl_2$ concentrations showed a nonlinear isosceles triangle shape. This indicated the favorable EDLC behavior with outstanding electrochemical reversibility, as shown in Fig. 10(a). The optimal GCD results were obtained for the PCE-0.3 sample with a triangular curve that was significantly greater with a longer charge–discharge time. This maximum time confirmed that the PCE-0.3

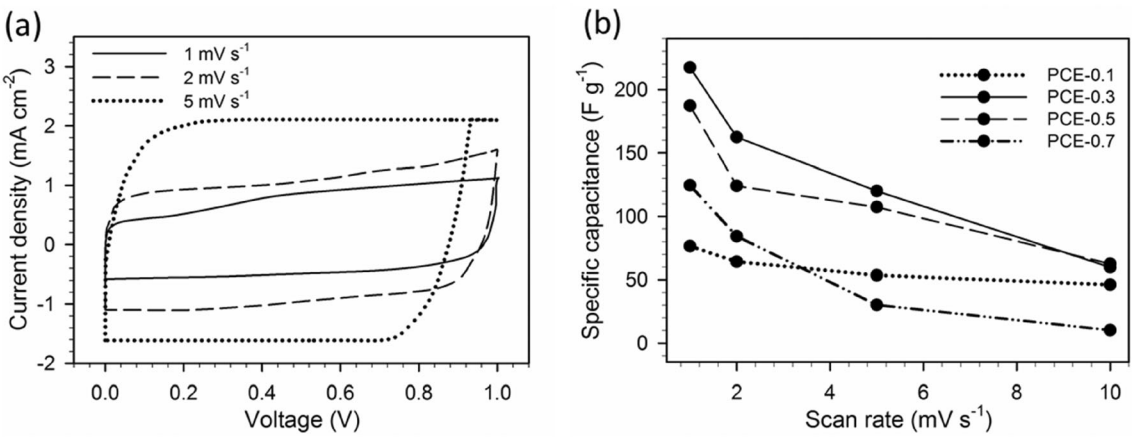

Figure 9. Effect of scan rate variations on PCE samples: (a) shape of the CV curve and (b) specific capacitance value.

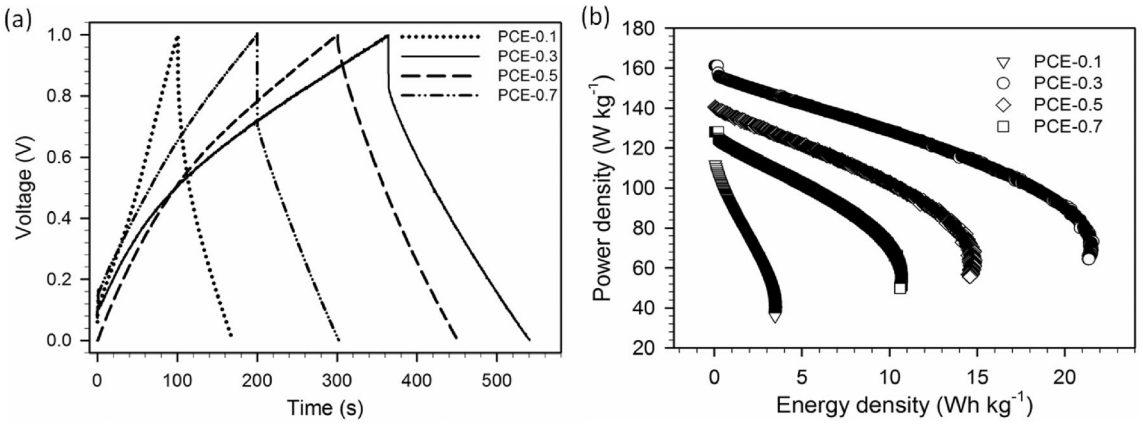

Figure 10. (a) Charge–discharge curves and (b) Ragone plot of PCE samples.

Table 3. Potential of PCE-0.3 electrode in energy storage and comparison with other samples

Sources	Electrode	Pore structure	Activator	Electrolyte	C_{sp} (F g^{-1})	E (Wh kg^{-1})	P (W kg^{-1})	R (Ω)	Ref.
Poplar sawdust	3	Honeycomb	—	6 mol L^{-1} KOH	348	—	—	0.66	21
Chingma abutilon seed	3	Honeycomb	KOH	Ionic	1719	95.29	802	0.26	60
Aloe peel	3	Honeycomb	KOH	6 mol L^{-1} KOH	264	—	—	—	74
Cork	2	Honeycomb	Na_2SO_4	6 mol L^{-1} KOH	102	42	750	—	75
PCE-0.3	2	Honeycomb	$ZnCl_2$	1 mol L^{-1} H_2SO_4	285.89	21.54	161.13	0.059	This study

electrode had the highest specific capacitance value, reaching 285.89 F g^{-1}. The slight hump-like bend in the charge current of the PCE-0.3 sample was due to a faradaic redox reaction, contributing to the pseudocapacitance properties[12,72,73] as described for the CV analysis. This was also attributed to the presence of a large number of participating micropores, increasing the active sites suitable for storage of charged ions which can improve the specific capacitance. The unique 3D pore structure such as a honeycomb rich in interconnected micropores was also advantageous for ion access in the carbon pores. Furthermore, the small *IR* drop at 1 A current confirmed the low internal resistance of the carbon material. As shown in Fig. 10(a), the specific capacitance decreased with the increase of $ZnCl_2$ activator concentration from optimum conditions. This was due to reduced amorphous porosity, wettability and surface area of activated carbon as presented in Fig. 10(b). The Ragon plot curve showed the relationship between the energy and power densities of all variations of the PCE electrode. Based on the electrochemical charge–discharge measurements, the maximum energy and power densities were exhibited by the PCE-0.3 electrode, with values of 21.54 Wh kg^{-1} and 161.13 W kg^{-1} with a small internal resistance of 0.059 Ω. The values of specific capacitance, energy density and power density were calculated from PCE samples based on differences in $ZnCl_2$ activator concentrations as described in Table 3. The measurements were carried out at a current density of 1 A and the values obtained were compared with those for previously reported biomass-derived carbon materials.

The electrochemical properties of activated carbon based on aromatic biomass waste ginger torch leaves at optimum conditions, i.e. PCE-03, were analyzed by the electrochemical impedance spectroscopy method. The tests were carried out in a two-electrode system with a 1 mol L^{-1} H_2SO_4 aqueous electrolyte, over a frequency range of 0.01 Hz to 100 MHz, with an amplitude constant of 10. The Nyquist plot confirmed the normal EDLC behavior for activated carbon materials from biomass as shown in Fig. 11(a). The diameter of the semicircle about the real axis (Z') in the high-frequency region represented the series resistance at charge transfer (R_{ct}) in the carbon material. The very small ESR value of the PCE-0.3 electrode 0.8 Ω also confirmed the suitability between the electrode and the electrolyte ions in increasing the active state. The small R_{ct} value of 13.6 Ω indicated the high conductivity of the material from the honeycomb-like 3D hierarchical pore structure rich in interconnected micropores. This R_{ct} was also related to good electrode wettability, compatible with 1 mol L^{-1} H_2SO_4 aqueous electrolyte, enabling efficient distribution of electrolyte ions through faradaic redox reactions at the interface of the suitable electrode and electrolyte. The Nyquist plot of PCE-0.3 showed the slope (Warburg element) identified at the 45° line in the low-frequency region. This confirmed the speed of the ion diffusion rate filling pores[76] to improve the electrochemical performance of supercapacitors with PCE-0.3 electrodes. Furthermore, the ideal capacitive behavior of PCE-0.3 was shown by the characteristics of ion diffusion at higher frequencies through the presence of an almost vertical curve. The high electrochemical performance of PCE-0.3 synergized with its interconnected 3D pore structure rich in microporosity. The Bode phase plot in Fig. 11(b) showing the phase angle close to −80° further confirmed the presence of real and imaginary capacitance in the material. Figure 11(c),(d) also revealed the real capacitance and imaginary capacitance parts, respectively, explaining the capacitive behavior at low frequency and relaxation

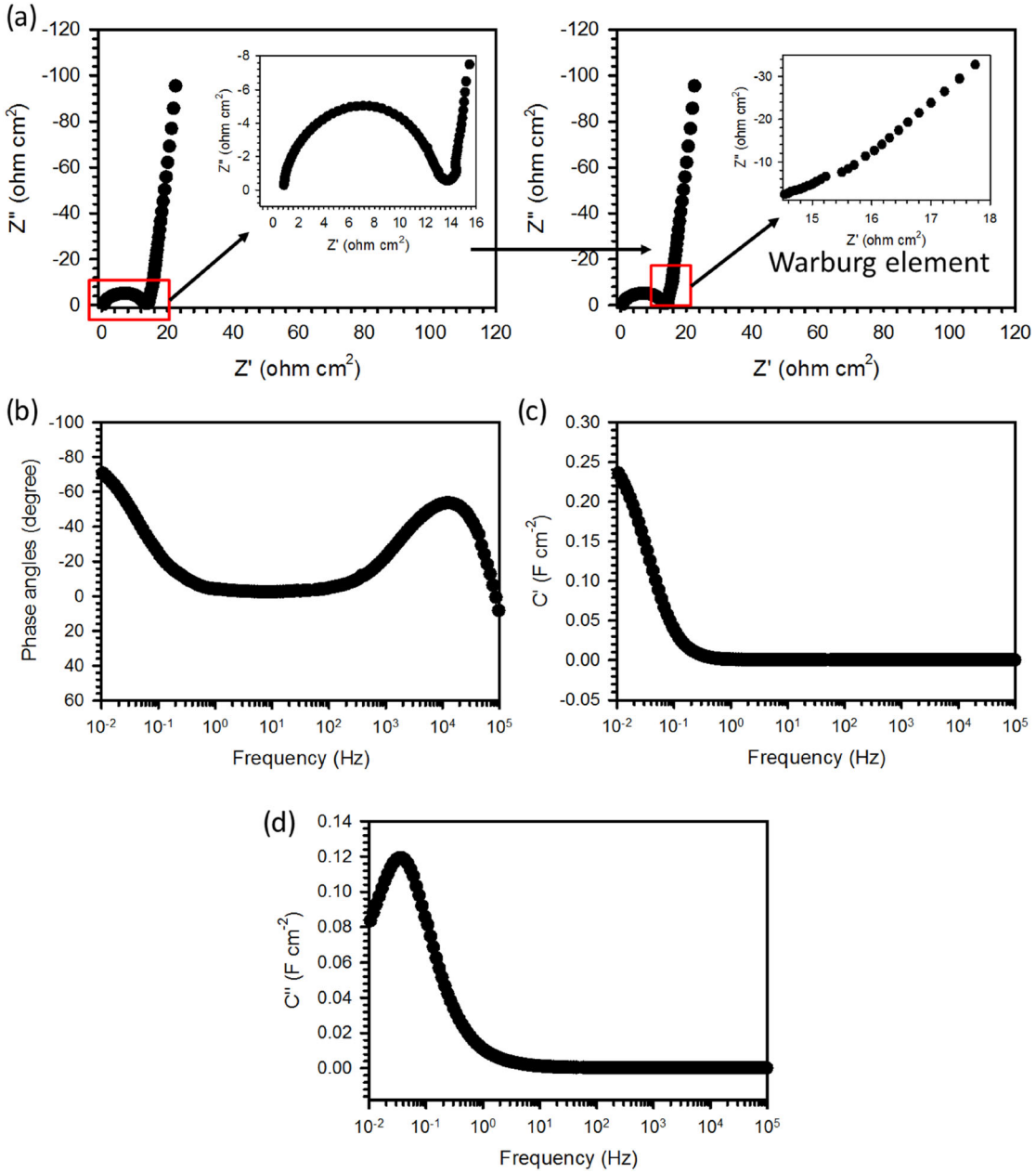

Figure 11. (a) Nyquist plot, (b) Bode phase plot, (c) Bode plot of real capacitance and (d) Bode plot of imaginary capacitance of PCE-03.

time. For a more detailed review regarding imaginary capacitance, the relaxation time of 8.33 s of the PCE-0.3 electrode was obtained using the equation $\tau = 1\ f_p^{-1}$.[77] The small relaxation time confirmed that the PCE-0.3 electrode based on aromatic biomass waste torch ginger leaves had a honeycomb-like 3D hierarchical pore structure. These electrodes are also rich in micropores with extraordinary ability, making them applicable as supercapacitor electrodes.

CONCLUSION

Supercapacitor cell components were fabricated using sustainable biomass of torch ginger (*Etlingera elatior* (Jack) R.M. Smith) leaves with 3D honeycomb-like morphology composed of microporous fibers from lignin and volatile compounds. This was achieved by impregnating the biomass waste with different concentrations of $ZnCl_2$ to create aromatic-based material. The activated carbon materials were synthesized using simple methods including chemical activation, carbonization and physical activation, which did not require complex equipment or cause damage to the environment. The porous carbon produced had a unique morphological structure with a high specific surface area of up to 519.02 $m^2\ g^{-1}$. Furthermore, the concentration level of $ZnCl_2$ impregnation was highly controlled in the synthesis process to obtain optimum conditions that affected electrochemical performance. The optimized activated carbon material, PCE-0.3 exhibited outstanding electrochemical performance with a specific capacitance reaching 285.89 F g^{-1} at 1 A. The supercapacitor also exhibited high energy density and power of 21.54 Wh kg^{-1} and 161.13 W kg^{-1}, respectively, with a low internal resistance of 0.059 Ω. These results suggested that activated carbon from

aromatic biomass waste, especially torch ginger leaves, is promising for sustainable, cost-effective and environmentally friendly energy storage for supercapacitor cell electrodes.

ACKNOWLEDGEMENTS

The research was financially supported by third years Project of Word Class Research (WCR) in Kementerian Pendidikan, Kebudayaan, Riset, dan Teknologi, Republic of Indonesia with the title 'Supercapacitors with high energy and power density: optimization of the electrode supply process', contract no. 11312/UN19.5.1.3/AL.04/2023.

DATA AVAILABILITY STATEMENT

The data that support the findings of this study are available from the corresponding author upon reasonable request.

REFERENCES

1 Kim M, Wang C, Earnshaw J, Park T, Amiralian N, Ashok A *et al.*, Correction: Co, Fe and N co-doped 1D assembly of hollow carbon nanoboxes for high-performance supercapacitors. *J Mater Chem A* **11**: 1511 (2022).
2 Salleh NA, Kheawhom S and Mohamad AA, Chitosan as biopolymer binder for graphene in supercapacitor electrode. *Results Phys* **25**: 104244 (2021). https://doi.org/10.1016/j.rinp.2021.104244.
3 Kigozi M, Kasozi GN, Balaso Mohite S, Zamisa S, Karpoormath R, Kirabira JB *et al.*, Non-emission hydrothermal low-temperature synthesis of carbon nanomaterials from poly(ethylene terephthalate) plastic waste for excellent supercapacitor applications. *Green Chem Lett Rev* **16**:2173025 (2023).
4 Han W, Yuan L, Liu X, Wang C and Li J, Ultrathin $MoSe_2$ nanosheets decorated on carbon aerogel microspheres for high-capacity supercapacitor electrodes. *J Electroanal Chem* **899**:115643 (2021). https://doi.org/10.1016/j.jelechem.2021.115643.
5 Bashir S, Hasan K, Hina M, Ali Soomro R, Mujtaba MA, Ramesh S *et al.*, Conducting polymer/graphene hydrogel electrodes based aqueous smart supercapacitors: a review and future prospects. *J Electroanal Chem.* **898**:115626 (2021). https://doi.org/10.1016/j.jelechem.2021.115626.
6 Wang J, Zheng F, Yu Y, Hu P, Li M, Wang J *et al.*, Symmetric supercapacitors composed of ternary metal oxides ($NiO/V_2O_5/MnO_2$) nanoribbon electrodes with high energy storage performance. *Chem Eng J* **426**:131804 (2021).
7 Du B, Zhu H, Chai L, Cheng J, Wang X, Chen X *et al.*, Effect of lignin structure in different biomass resources on the performance of lignin-based carbon nanofibers as supercapacitor electrode. *Ind Crops Prod* **170**:113745 (2021). https://doi.org/10.1016/j.indcrop.2021.113745.
8 Zhang Y, Sun J, Tan J, Ma CH, Luo S, Li W *et al.*, Multi-walled carbon nanotubes/carbon foam nanocomposites derived from biomass for CO_2 capture and supercapacitor applications. *Fuel* **305**:121622 (2021). https://doi.org/10.1016/j.fuel.2021.121622.
9 He D, Gao Y, Wang Z, Yao Y, Wu L, Zhang J *et al.*, One-step green fabrication of hierarchically porous hollow carbon nanospheres (HCNSs) from raw biomass: formation mechanisms and supercapacitor applications. *J Colloid Interface Sci* **581**:238–250 (2021).
10 Taer E, Yanti N, Mustika WS, Apriwandi A, Taslim R and Agustino A, Porous activated carbon monolith with nanosheet/nanofiber structure derived from the green stem of cassava for supercapacitor application. *Int J Energy Res* **44**:10192–10205 (2020).
11 Zhang M, Igalavithana AD, Xu L, Sarkar B, Hou D, Zhang M *et al.*, Engineered/designer hierarchical porous carbon materials for organic pollutant removal from water and wastewater: a critical review. *Crit Rev Environ Sci Technol.* **51**:2295–2328 (2021). https://doi.org/10.1080/10643389.2020.1780102.
12 Wang Y, Liu R, Tian Y, Sun Z, Huang Z, Wu X *et al.*, Heteroatoms-doped hierarchical porous carbon derived from chitin for flexible all-solid-state symmetric supercapacitors. *Chem Eng J* **384**:123263 (2020). https://doi.org/10.1016/j.cej.2019.123263.
13 Du W, Wang X, Zhan J, Sun X, Kang L, Jiang F *et al.*, Biological cell template synthesis of nitrogen-doped porous hollow carbon spheres/MnO_2 composites for high-performance asymmetric supercapacitors. *Electrochim Acta* **296**:907–915 (2019). https://doi.org/10.1016/j.electacta.2018.11.074.
14 Zhang W, Lin H, Lin Z, Yin J, Lu H, Liu D *et al.*, 3D hierarchical porous carbon for supercapacitors prepared from lignin through a facile template-free method. *ChemSusChem* **8**:2114–2122 (2015).
15 Igalavithana AD, Mandal S, Niazi NK, Vithanage M, Parikh SJ, Mukome FND *et al.*, Advances and future directions of biochar characterization methods and applications. *Crit Rev Environ Sci Technol* **47**: 2275–2330 (2017). https://doi.org/10.1080/10643389.2017.1421844.
16 Huang J, Wu J, Dai F and Li CM, 3D honeycomb-like carbon foam synthesized with biomass buckwheat flour for high-performance supercapacitor electrodes. *Chem Commun* **55**:9168–9171 (2019).
17 Jiang H, Lee PS and Li C, 3D carbon based nanostructures for advanced supercapacitors. *Energ Environ Sci* **6**:41–53 (2013).
18 Kim M, Firestein KL, Fernando JFS, Xu X, Lim H, Golberg DV *et al.*, Strategic design of Fe and N co-doped hierarchically porous carbon as superior ORR catalyst: from the perspective of nanoarchitectonics. *Chem Sci* **13**:10836–10845 (2022).
19 Kim M, Xu X, Xin R, Earnshaw J, Ashok A, Kim J *et al.*, KOH-activated hollow ZIF-8 derived porous carbon: nanoarchitectured control for upgraded capacitive deionization and Supercapacitor. *ACS Appl Mater Interfaces* **44**:52034–52043 (2021).
20 Kim M, Fernando JFS, Li Z, Alowasheeir A, Ashok A, Xin R *et al.*, Ultrastable sodium ion storage of biomass porous carbon derived from sugarcane. *Chem Eng J* **445**:136344 (2022).
21 Cao M, Wang Q, Cheng W, Huan S, Hu Y, Niu Z *et al.*, A novel strategy combining electrospraying and one-step carbonization for the preparation of ultralight honeycomb-like multilayered carbon from biomass-derived lignin. *Carbon* **179**:68–79 (2021).
22 Taer E, Effendi NY, Taslim R and Apriwandi A, Interconnected micro-mesoporous carbon nanofiber derived from lemongrass for high symmetric supercapacitor performance. *J Mater Res Technol* **19**: 4721–4732 (2022). https://doi.org/10.1016/j.jmrt.2022.06.167.
23 Bhattacharya M, Srivastav PP and Mishra HN, Optimization of process variables for supercritical fluid extraction of ergothioneine and polyphenols from *Pleurotus ostreatus* and correlation to free-radical scavenging activity. *J Supercrit Fluids* **95**:51–59 (2014). https://doi.org/10.1016/j.supflu.2014.07.031.
24 Tao NG and Liu YJ, Chemical composition and antimicrobial activity of the essential oil from the peel of *Shatian pummelo* (citrus Grandis Osbeck). *Int J Food Prop* **15**:709–716 (2012).
25 Jackie T, Haleagrahara N and Chakravarthi S, Antioxidant effects of *Etlingera elatior* flower extract against lead acetate-induced perturbations in free radical scavenging enzymes and lipid peroxidation in rats. *BMC Res Notes* **4**(1):67–0 (2011). https://doi.org/10.1186/1756-0500-4-67
26 Choon SY and Ding P, Developmental changes in cellular structure and cell wall metabolism of torch ginger (*Etlingera elatior* (Jack) R.M. Smith) inflorescence. *Curr Plant Biol* **9–10**:3–10 (2017). https://doi.org/10.1016/j.cpb.2017.01.001.
27 Ge L, Yong JWH, Tan SN and Li SP, Simultaneous extraction, separation, isolation and identification of endogenous components from *Etlingera elatior* by pressurized matrix solid-phase dispersion using liquid chromatography–mass spectrometry. *J Chromatogr A* **1611**:460604 (2020). https://doi.org/10.1016/j.chroma.2019.460604.
28 Marzlan AA, Muhialdin BJ, Zainal Abedin NH, Mohammed NK, Abadl MMT, Mohd Roby BH *et al.*, Optimized supercritical CO_2 extraction conditions on yield and quality of torch ginger (*Etlingera elatior* (Jack) R.M. Smith) inflorescence essential oil. *Ind Crops Prod* **154**:112581 (2020). https://doi.org/10.1016/j.indcrop.2020.112581.
29 Wang T, Xu Y, Shi B, Gao S, Meng G and Huang K, Novel activated N-doped hollow microporous carbon nanospheres from pyrrole-based hyper-crosslinking polystyrene for supercapacitors. *React Funct Polym* **143**:104326 (2019). https://doi.org/10.1016/j.reactfunctpolym.2019.104326.
30 Wan L, Hu J, Liu J, Xie M, Zhang Y, Chen J *et al.*, Heteroatom-doped porous carbons derived from lotus pollen for supercapacitors: comparison of three activators. *J Alloys Compd* **859**:158390 (2021). https://doi.org/10.1016/j.jallcom.2020.158390.
31 González-García P, Activated carbon from lignocellulosics precursors: a review of the synthesis methods, characterization techniques and applications. *Renew Sustain Energy Rev* **82**:1393–1414 (2018). https://doi.org/10.1016/j.rser.2017.04.117.

32 Taer E, Yanti N, Putri JA, Apriwandi A and Taslim R, Novel macaroni-sponge-like pore structure biomass (*Zingiber officinale* Rosc. leaves)-based electrode material for excellent energy gravimetric supercapacitor. *J Chem Technol Biotechnol* **2022**:990–1002 (2022).
33 Taer E, Apriwandi W, Taslim R and Deraman M, Novel laurel aromatic evergreen biomass derived hierarchical porous carbon nanosheet as sustainable electrode for high performance symmetric supercapacitor. *J Energy Storage.* **67**:107567 (2023). https://doi.org/10.1016/j.est.2023.107567.
34 Wei Q, Chen Z, Cheng Y, Wang X, Yang X and Wang Z, Preparation and electrochemical performance of orange peel based-activated carbons activated by different activators. *Colloids Surf A* **574**:221–227 (2019). https://doi.org/10.1016/j.colsurfa.2019.04.065.
35 Wang Y, Qu Q, Gao S, Tang G, Liu K, He S *et al.*, Biomass derived carbon as binder-free electrode materials for supercapacitors. *Carbon* **155**: 706–726 (2019). https://doi.org/10.1016/j.carbon.2019.09.018.
36 Shi M, Xin Y, Chen X, Zou K, Jing W, Sun J *et al.*, Coal-derived porous activated carbon with ultrahigh specific surface area and excellent electrochemical performance for supercapacitors. *J Alloys Compd* **859**:157856 (2021). https://doi.org/10.1016/j.jallcom.2020.157856.
37 Apriwandi A, Taer E, Farma R, Setiadi RN and Amiruddin E, A facile approach of micro-mesopores structure binder-free coin/monolith solid design activated carbon for electrode supercapacitor. *J Energy Storage.* **40**:102823 (2021). https://doi.org/10.1016/j.est.2021.102823.
38 Taer E, Syamsunar N, Apriwandi A and Taslim R, Novel solanum torvum fruit biomass-derived hierarchical porous carbon nanosphere as excellent electrode material for enhanced symmetric Supercapacitor performance. *JOM* (2023). https://doi.org/10.1007/s11837-023-05801-x.
39 Taer E, Apriwandi A, Chow S and Taslim R, Integrated pyrolysis approach of self-O-doped hierarchical porous carbon volumetric performance. *Diam Relat Mater J* **135**:109866 (2023).
40 Shoaib M and Al-Swaidan HM, Optimization and characterization of sliced activated carbon prepared from date palm tree fronds by physical activation. *Biomass Bioenergy* **73**:124–134 (2015). https://doi.org/10.1016/j.biombioe.2014.12.016.
41 Riyanto CA, Ampri MS and Martono Y, Synthesis and characterization of nano activated carbon from annatto peels (*Bixa orellana* L.) viewed from temperature activation and impregnation ratio of H_3PO_4. *EKSAKTA J Sci Data Anal* **2**:44–50 (2020).
42 Saka C, BET, TG-DTG, FT-IR, SEM, iodine number analysis and preparation of activated carbon from acorn shell by chemical activation with $ZnCl_2$. *J Anal Appl Pyrolysis* **95**:21–24 (2012). https://doi.org/10.1016/j.jaap.2011.12.020.
43 Tang YB, Liu Q and Yan CF, Preparation and characterization of activated carbon from waste ramulus mori. *Chem Eng J* **203**:19–24 (2012). https://doi.org/10.1016/j.cej.2012.07.007.
44 Baig MM and Gul IH, Conversion of wheat husk to high surface area activated carbon for energy storage in high-performance supercapacitors. *Biomass Bioenergy* **144**:105909 (2021). https://doi.org/10.1016/j.biombioe.2020.105909.
45 Cao L, Li H, Xu Z, Zhang H, Ding L, Wang S *et al.*, Comparison of the heteroatoms-doped biomass-derived carbon prepared by one-step nitrogen-containing activator for high performance supercapacitor. *Diam Relat Mater* **114**:108316 (2021). https://doi.org/10.1016/j.diamond.2021.108316.
46 Qu H, Zhang X, Zhan J, Sun W, Si Z and Chen H, Biomass-based nitrogen-doped hollow carbon nanospheres derived directly from glucose and glucosamine: structural evolution and supercapacitor properties. *ACS Sustain Chem Eng* **6**:7380–7389 (2018).
47 Márquez-Montesino F, Torres-Figueredo N, Lemus-Santana A and Trejo F, Activated carbon by potassium carbonate activation from pine sawdust (*Pinus montezumae* lamb.). *Chem Eng Technol* **43**: 1716–1725 (2020).
48 Lin XQ, Lü QF, Li Q, Wu M and Liu R, Fabrication of low-cost and eco-friendly porous biocarbon using Konjaku flour as the raw material for high-performance supercapacitor application. *ACS Omega* **3**: 13283–13289 (2018).
49 Yang H, Sun X, Zhu H, Yu Y, Zhu Q, Fu Z *et al.*, Nano-porous carbon materials derived from different biomasses for high performance supercapacitors. *Ceram Int* **46**:5811–5820 (2020). https://doi.org/10.1016/j.ceramint.2019.11.031.
50 Zhu J, Yan C, Zhang X, Yang C, Jiang M and Zhang X, A sustainable platform of lignin: from bioresources to materials and their applications in rechargeable batteries and supercapacitors. *Prog Energy Combust Sci* **76**:100788 (2020). https://doi.org/10.1016/j.pecs.2019.100788.
51 Guo N, Li M, Sun X, Wang F and Yang R, Enzymatic hydrolysis lignin derived hierarchical porous carbon for supercapacitors in ionic liquids with high power and energy densities. *Green Chem* **19**:2595–2602 (2017).
52 Zheng LH, Chen MH, Liang SX and Lü QF, Oxygen-rich hierarchical porous carbon derived from biomass waste-kapok flower for supercapacitor electrode. *Diam Relat Mater* **113**:108267 (2021). https://doi.org/10.1016/j.diamond.2021.108267.
53 Chen W, Wang H, Lan W, Li D, Zhang A and Liu C, Construction of sugarcane bagasse-derived porous and flexible carbon nanofibers by electrospinning for supercapacitors. *Ind Crops Prod* **170**:113700 (2021).
54 Han G, Jia J, Liu Q, Huang G, Xing B, Zhang C *et al.*, Template-activated bifunctional soluble salt $ZnCl_2$ assisted synthesis of coal-based hierarchical porous carbon for high-performance supercapacitors. *Carbon* **186**:380–390 (2022). https://doi.org/10.1016/j.carbon.2021.10.042.
55 Yaglikci S, Gokce Y, Yagmur E and Aktas Z, The performance of sulphur doped activated carbon supercapacitors prepared from waste tea. *Environ Technol* **41**:36–48 (2020). https://doi.org/10.1080/09593330.2019.1575480.
56 Wang J, Xu Y, Yan M, Ren B, Dong X, Miao J *et al.*, Preparation and application of biomass-based porous carbon with S, N, Zn, and Fe heteroatoms loading for use in supercapacitors. *Biomass Bioenergy* **156**: 106301 (2022). https://doi.org/10.1016/j.biombioe.2021.106301.
57 Xie XB, Zhang B, Wang Q, Zhao X, Wu D, Wu H *et al.*, Efficient microwave absorber and supercapacitors derived from puffed-rice-based biomass carbon: effects of activating temperature. *J Colloid Interface Sci* **594**:290–303 (2021). https://doi.org/10.1016/j.jcis.2021.03.025.
58 Kanjana K, Harding P, Kwamman T, Kingkam W and Chutimasakul T, Biomass-derived activated carbons with extremely narrow pore size distribution via eco-friendly synthesis for supercapacitor application. *Biomass Bioenergy.* **153**:106206 (2021). https://doi.org/10.1016/j.biombioe.2021.106206.
59 Hu SC, Cheng J, Wang WP, Sun GT, Le HL, Zhu MQ *et al.*, Structural changes and electrochemical properties of lacquer wood activated carbon prepared by phosphoric acid-chemical activation for supercapacitor applications. *Renew Energy* **177**:82–94 (2021).
60 Ma M, Cai W, Chen Y, Li Y, Tan F and Zhou J, Flower-like NiMn-layered double hydroxide microspheres coated on biomass-derived 3D honeycomb porous carbon for high-energy hybrid supercapacitors. *Ind Crops Prod* **166**:113472 (2021). https://doi.org/10.1016/j.indcrop.2021.113472.
61 Wang Q, Lai Z, Luo C, Zhang J, Cao X, Liu J *et al.*, Honeycomb-like activated carbon with microporous nanosheets structure prepared from waste biomass cork for highly efficient dye wastewater treatment. *J Hazard Mater* **416**:125896 (2021). https://doi.org/10.1016/j.jhazmat.2021.125896.
62 Tobi AR and Dennis JO, Activated carbon from composite of palm biowaste as electrode material for solid-state electric double layer capacitor. *J Energy Storage* **42**:103087 (2021). https://doi.org/10.1016/j.est.2021.103087.
63 Liu Z, Hu J, Shen F, Tian D, Huang M, He J *et al.*, Trichoderma bridges waste biomass and ultra-high specific surface area carbon to achieve a high-performance supercapacitor. *J Power Sources* **497**: 229880 (2021). https://doi.org/10.1016/j.jpowsour.2021.229880.
64 Jain A, Ghosh M, Krajewski M, Kurungot S and Michalska M, Biomass-derived activated carbon material from native European deciduous trees as an inexpensive and sustainable energy material for supercapacitor application. *J Energy Storage* **34**:102178 (2021). https://doi.org/10.1016/j.est.2020.102178.
65 Wang L, Sun F, Gao J, Pi X, Pei T, Qie Z *et al.*, A novel melt infiltration method promoting porosity development of low-rank coal derived activated carbon as supercapacitor electrode materials. *J Taiwan Inst Chem Eng* **91**:588–596 (2018). https://doi.org/10.1016/j.jtice.2018.06.014.
66 Jin ZY, Lu AH, Xu YY, Zhang JT and Li WC, Ionic liquid-assisted synthesis of microporous carbon nanosheets for use in high rate and long cycle life supercapacitors. *Adv Mater* **26**:3700–3705 (2014).
67 Wang M, Liu B, Chen H, Yang D and Li H, N/O codoped porous carbons with layered structure for high-rate performance supercapacitors. *ACS Sustain Chem Eng.* **7**:11219–11227 (2019).
68 Shi L, Ye J, Lu H, Wang G, Lv J and Ning G, Flexible all-solid-state supercapacitors based on boron and nitrogen-doped carbon network

anchored on carbon fiber cloth. *Chem Eng J* **410**:128365 (2021). https://doi.org/10.1016/j.cej.2020.128365.
69 Chen H, Zheng Y, Zhu X, Hong W, Tong Y, Lu Y *et al*., Bamboo-derived porous carbons for Zn-ion hybrid supercapacitors. *Mater Res Bull* **139**: 111281 (2021). https://doi.org/10.1016/j.materresbull.2021.111281.
70 Maron GK, Alano JH, da Silveira NB, da Silva RL, Stolojan V, Silva SRP *et al*., Electrochemical supercapacitors based on 3D nanocomposites of reduced graphene oxide/carbon nanotube and ZnS. *J Alloys Compd* **836**:155408 (2020).
71 Dong X, Wang J, Yan M, Ren B, Miao J, Zhang L *et al*., Hierarchically Fe-doped porous carbon derived from phenolic resin for high performance supercapacitor. *Ceram Int* **47**:5998–6009 (2021). https://doi.org/10.1016/j.ceramint.2020.10.175.
72 Lai F, Miao YE, Zuo L, Lu H, Huang Y and Liu T, Biomass-derived nitrogen-doped carbon nanofiber network: a facile template for decoration of ultrathin nickel-cobalt layered double hydroxide nanosheets as high-performance asymmetric supercapacitor electrode. *Small* **12**:3235–3244 (2016).
73 Shao X, Zhu Z, Zhao C, Zhao C and Qian X, Hierarchical FeS/-RGO/FeS@Fe foil as high-performance negative electrode for asymmetric supercapacitors. *Inorg Chem Front* **5**:1912–1922 (2018).
74 Lei E, Sun J, Gan W, Wu Z, Xu Z, Xu L *et al*., N-doped cellulose-based carbon aerogels with a honeycomb-like structure for high-performance supercapacitors. *J Energy Storage* **38**:102414 (2021). https://doi.org/10.1016/j.est.2021.102414.
75 Mitravinda T, Anandan S, Sharma CS and Rao TN, Design and development of honeycomb structured nitrogen-rich cork derived nanoporous activated carbon for high-performance supercapacitors. *J Energy Storage* **34**:102017 (2021). https://doi.org/10.1016/j.est.2020.102017.
76 Shi J, Haegeman W and Andries J, Investigation on the mechanical properties of a calcareous sand: the role of the initial fabric. *Mar Georesources Geotechnol* **39**:859–875 (2021). https://doi.org/10.1080/1064119X.2020.1775327.
77 Shu Y, Bai Q, Fu G, Xiong Q, Li C, Ding H *et al*., Hierarchical porous carbons from polysaccharides carboxymethyl cellulose, bacterial cellulose, and citric acid for supercapacitor. *Carbohydr Polym* **227**:115346 (2020). https://doi.org/10.1016/j.carbpol.2019.115346.

